Electrical Control of Spin-Injection Using Mixed Dimensional van der Waals Heterostructures

John Eric Tiessen and Junxia Shi, *Senior Member, IEEE*

***Abstract*—We demonstrate that van der Waals heterostructures based on CrI_3, MoS_2 and a 3D semiconductor source may allow for all electrical control of spin polarized carrier injection into MoS_2. We demonstrate this possibility using a simple resonant tunneling device structure and model it using the transfer matrix method. Our results show that electrically controlled spin polarized carrier injection is theoretically possible at low device bias.**

***Index Terms*—2D materials, CrI_3, MoS_2, $In_xGa_{1-x}N$, GaN, mixed dimensional structures, spin-polarization, van der waals heterostructures.**

I. Introduction

THE control of spin polarized carrier injection is of great importance to the fields of spintronics and valleytronics, which seek to use the spin of carriers as an additional degree of freedom in device design. Effective control over the spin of carriers in a device can lead to a variety of useful device applications such as nonvolatile memory and quantum computing [1], [2]. Having good control over the initial spin of carriers is an important part of practical quantum computing with 2D materials. Transition metal dichalcogenides (TMDCs) especially can take advantage of spin-polarized carriers since carriers of different spins populate different valleys within their conduction band. Therefore, researching spin-injection and control into TMDCs is of great practical importance in the application of TMDC based devices. One of the most popular approaches to spin injection and control in TMDCs is that of Magnetic Tunnel Junctions (MTJs) using different magnetic metal contacts [3], [4]. However, a major problem with this method is conductivity mismatch which results in poor spin injection [5], [6]. Spin polarized light is another method of spin-injection [7] which although effective at creating significant populations of spin polarized carriers in TMDCs, is impractical in terms of device design and implementation. Finally, there is proximity spin filtering [8] where a 2D magnetic material such as CrI_3 is placed on top of a TMDC to lift the valley degeneracy of the TMDC layer and create a net spin-polarized carrier population. However, both proximity spin filtering and MTJs have the same problem with requiring external magnetic fields to change carrier selection.

To get around these limitations, we propose a Resonant Tunneling Device (RTD) to control the injection of spin polarized carriers. This method of spin injection was previously proposed, developed and tested in $Zn_{1-x}Mn_xSe$ based structures in [9] and [10]. A similar concept was employed in [11] using $Zn_{1-x-y}Mn_yCd_xSe$ instead of $Zn_{1-x}Mn_xSe$. In our proposed device, we intend to use a 2D/3D van der Waals (vdW) heterostructure to overcome the limitations traditionally associated with spin dependent RTDs. One way in which we intend to improve upon spin dependent RTDs is to use CrI_3, a novel 2D magnetic material, as the well material. The unique properties of layered 2D materials in conjunction with the well understood physics of bulk semiconductors allow us to conceive of and simulate a device which can select the spin of carriers using all electric means.

II. Device Concept

Our proposed spin RTD consists of six parts, a bulk semiconductor source, one or two barrier layers, a magnetic well material, a TMDC drain, an insulator and finally a back-gate material made of either metal or highly doped semiconductor. A simplified diagram of the electronic structure of the device can be seen in Fig. 1. It should be noted that in Fig. 1, the conduction band of MoS_2 is represented with the Γ-point value of the MoS_2 band structure instead of the conduction band minimum (CBM). This is done to maintain momentum conservation for the carriers as they move from the 3D semiconductor source to the TMDC layer. The limiting factor in the design of spin-RTDs is the magnetic well material. This was one of the major problems with spin-RTDs which used $Zn_{1-x}Mn_xSe$ since the difference in the energy of spin polarized carriers within the well of the RTD was not large enough to create highly spin-polarized currents.

The spin splitting in $Zn_{1-x}Mn_xSe$ was expected to be on the order of 0.02 eV [9], [10] which means that the well could not effectively filter out one spin state from another, as both spin polarizations had similar probabilities of tunneling through the structure due to the closeness of their resonant states within the well. Using a combination of new device concepts, 2D/3D heterostructures, in conjunction with novel 2D magnetic materials, CrI_3, it may be possible to overcome some of the limitations of spin RTDs.

CrI_3 is a recently isolated 2D magnetic material which has been shown experimentally to behave ferromagnetically (FM) in

Manuscript received April 14, 2020; revised July 26, 2020; accepted September 16, 2020. Date of publication September 21, 2020; date of current version October 6, 2020. This work was sponsored by the Army Research Office and was accomplished under Grant Number W911NF-19-1-0309. The review of this article was arranged by Associate Editor Dr. Yoshikazu Hirai. *(Corresponding author: Junxia Shi.)*

The authors are with the Department of Electrical and Computer Engineering, University of Illinois at Chicago, Chicago, IL 60607 USA (e-mail: tiessen2@uic.edu; lucyshi@uic.edu).

Digital Object Identifier 10.1109/TNANO.2020.3025481

This work is licensed under a Creative Commons Attribution 4.0 License. For more information, see https://creativecommons.org/licenses/by/4.0/

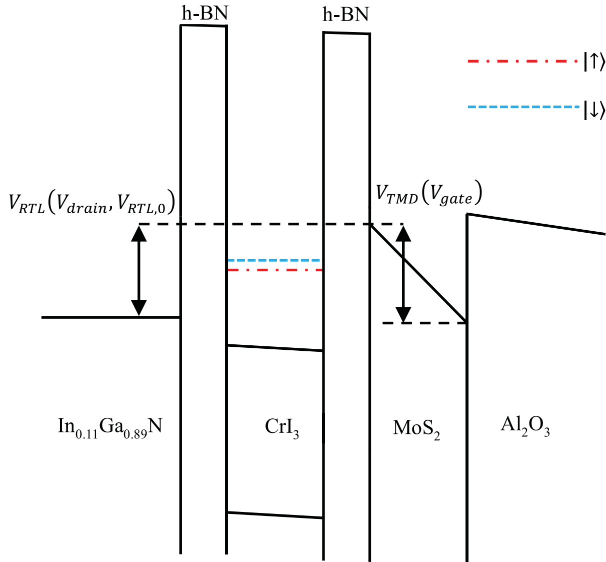

Fig. 1. Band diagram of the double h-BN barrier spin-RTD at -0.25 $\boldsymbol{V_{drain}}$ and 15 $\boldsymbol{V_{gate}}$. Equations (7)-(12) are used in calculating the movement of the conduction bands.

the monolayer limit and anti-ferromagnetically (AFM) in multilayers [12]. CrI_3 has been reported to have an exchange-induced energy gap of up to 0.136 eV [13], which indicates that carriers of different spin polarizations can have their energy differ by up to 0.136 eV in the presence of CrI_3. This is almost an order of magnitude larger than the energy splitting experienced by carriers in previously studied magnetic RTD materials [9]–[11]. In our proposed device, we only use a single layer of CrI_3 due to multiple layers of CrI_3 having AFM alignment, which would require an external magnetic field to operate. Alternatively, other 2D magnetic materials could be used, which have FM ordering in their layered stacks such as $CrBr_3$ [14], [15], therefore allowing for a wider well structure. The barriers of our proposed RTD are made of hexagonal Boron Nitride (h-BN), which act to protect the CrI_3 from oxidation as well as extremely tall and thin tunneling barriers for the RTD. The source and drain of the device would be constructed using $In_xGa_{1-x}N$ and MoS_2 respectively. This means that the device would take advantage of some of the useful properties of 2D/3D heterostructures which have recently been experimentally demonstrated [16]–[19].

Our expectation that resonant tunneling can occur in 2D/3D heterostructures is based on recent work in understanding the nature of electrostatically gated contacts with TMDCs [20]–[22]. In all these papers, the authors either assume, or determine through DFT calculations, that the carriers which dominate the tunneling current in metal/insulator/TMDC structures are carriers which travel perpendicular to the 2D/3D interface. In other words, carriers which are traveling vertically through the structure and into the TMDC layer are the ones responsible for most of the observed current in a gated metal/insulator/TMDC system. Furthermore, these authors can fit their I-V data with theories which are effectively modified versions of Schottky barrier tunneling [20], [21]. Therefore, this suggests that classic tunneling theory can be effectively applied to the study of gated metal/insulator/TMDC devices. Since these classic theories of tunneling through Schottky barriers are similar in their assumptions to theories of resonant tunneling, it does not seem unreasonable to assume that classic resonant tunneling is possible in 2D/3D heterostructures. In fact, the potential of layered vdW heterostructures to form RTDs has also been noted previously [23] and has been experimentally demonstrated by others [24], [25].

In a spin RTD, the depth of the well changes based on the spin polarization of the incident carrier. This spin dependence is due to the magnetic nature of the well material and results in an energy splitting between spin-up, $|\uparrow\rangle$, and spin-down, $|\downarrow\rangle$, states. The difference in energy between $|\uparrow\rangle$ and $|\downarrow\rangle$ in the magnetic material is the exchange-induced energy gap and will be referred to as E_{ex}. For example, if the carrier is $|\uparrow\rangle$ when it enters the well, the depth of the well will either be increased or decreased by $E_{ex}/2$ depending on if the spin is aligned or anti-aligned with the magnetic well layer, thus there are two sets of resonant tunneling energies. The goal of our device design is to make it possible to select the spin of the carrier which is preferentially transmitted. Selecting spin can be done by changing the electron affinity of the source, applying a drain bias, changing the electrostatic gate bias or a combination of all three.

III. Simulation Setup

The first step in simulating the band alignment of the various materials in the spin RTD is to determine their initial relative position when there is no applied drain or gate bias. In [21] this was done by comparing the electron affinities of the different materials. This works well for metals but if the source is a semiconductor, such as $In_xGa_{1-x}N$, it is more reasonable to determine the initial band alignment between materials by comparing Fermi-levels. For the devices under consideration, we will assume that the semiconductor source is degenerately n-type doped and for simplicity that the Fermi-level is set equal to the conduction band minimum of the source. It has been shown experimentally that it is possible to dope group III-nitrides heavily, or even degenerately, n-type using either silicon or germanium as donors in [26]–[29]. For example, in [26] the Fermi-level of n-type GaN was found to vary from 133.9 meV below the CB to 153.3 meV above the CB with Si doping concentrations ranging from $0.01 \times 10^{18} cm^{-3}$ to $23 \times 10^{18} cm^{-3}$. Even higher doping concentrations using Ge were demonstrated in [27]–[29] and therefore it is reasonable to assume that moving the Fermi-level to the conduction band edge should be experimentally feasible. Furthermore, since we will only be using $In_xGa_{1-x}N$ with an indium composition of 11%, it should be possible to use same doping to achieve a similar result [30]. Since the bulk semiconductor in either case will be degenerately doped, we will further assume that the Fermi-level in the source does not change and that the Fermi-level in the TMDC layer is equal to that of the source layer when the system is at thermal equilibrium.

As charge is transferred from the degenerately doped 3D semiconductor to the 2D TMDC, an electric field is created due to the

ionized dopants in the 3D source and the build-up of electrons in the TMDC drain layer. Using the depletion approximation and treating the source and TMDC layers as parallel plates in a capacitor, the electric field across the insulating resonant tunneling layers (RTLs) can be calculated using (1).

$$\vec{E} = -\frac{q}{2\epsilon_0\epsilon_{RTL}}\left(n_{source} - N_{TMD}\right) \quad (1)$$

In (1), q is the charge of the carrier, ϵ_0 is the dielectric permittivity of vacuum, ϵ_{RTL} is the effective dielectric constant of the RTLs, n_{source} is the ionized dopant concentration in the source layer at equilibrium while N_{TMD} is the number of carriers added to the TMDC layer from the source. N_{TMD} is a consequence of the depletion approximation applied to a 2D/3D heterostructure. For the Fermi-level in the TMDC layer to be brought into thermal equilibrium with that of the source, carriers must be transferred from the source material to the TMDC layer. Since all the carriers added to the TMDC layer come from the source in our model, at equilibrium we have a charge balance between the source ($In_xGa_{1-x}N$ /GaN) and the drain (TMDC), $n_{source} = -N_{TMD}$. We also expect N_{TMD} to be equal to the difference in carrier concentration in the TMDC layer before and after contact with the 3D semiconductor as expressed by (2).

$$N_{TMD} = n_{TMD}\left(E_C, E_{Fs}\right) - n_{TMD}\left(E_{Ci}, E_{Fi}\right) \quad (2)$$

Where $n_{TMD}(E_C, E_{Fs})$ is the number of carriers (electrons) expressed in carriers per cm^2 for a given conduction band energy (E_C) and the Fermi-level of the source (E_{Fs}). It is assumed that the final position of the Fermi-level in the TMDC drain will be equal to that of the source at thermal equilibrium. $n_{TMD}(E_{Ci}, E_{Fi})$ is the same as $n_{TMD}(E_C, E_{Fs})$ except E_{Ci} and E_{Fi} are the intrinsic, or starting, values of the TMDC conduction band energy and Fermi-level. The equations for n_{TMD} come from [31] and is defined using (3)-(5).

$$n\ (E_C, E_F) = g_{2D}\ k_B T \ln\left[1 + Exp\left(\frac{[E_F - E_C]}{k_B T}\right)\right] \quad (3)$$

$$p\ (E_C, E_F) = g_{2D}\ k_B T \ln \times \left[1 + Exp\left(\frac{-[E_F - (E_C - E_g)]}{k_B T}\right)\right] \quad (4)$$

$$n_{TMD}\ (E_C, E_F) = n\left(E_C, E_F\right) - p\left(E_C, E_F\right) \quad (5)$$

In (3) and (4) which go into (5), T is the temperature in Kelvin, k_B is Boltzmann's constant and g_{2D} is the 2D density of states which can be written down in (6).

$$g_{2D} = g_s g_v m_e / 2\pi\hbar^2 \quad (6)$$

Where in (6) g_s is the spin-degeneracy of the TMDC and g_v is the valley degeneracy. In our case both are equal to 2 during device operation. Using (1) and (2), the built-in potential for electrons over the RTLs can be calculated as follows:

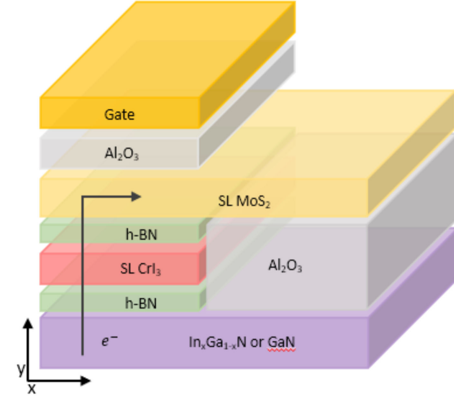

Fig. 2. Double h-BN barrier spin-RTD device structure. The CrI_3 layer is assumed to be magnetically polarized in the +y direction. The single h-BN barrier device structure is the same but with the h-BN layer between the CrI_3 and MoS_2 layers removed. The gate voltage, V_{gate}, drops over the top Al_2O_3 gate dielectric layer and the MoS_2 monolayer. The drain bias, V_{drain}, is the applied bias measured between the $In_xGa_{1-x}N$/GaN layer and the MoS_2 layer.

$$q\,V_{RTL} = \frac{q^2 t_{RTL}}{2\epsilon_0\epsilon_{RTL}}\left(2\left[n_{TMD}\left(E_C, E_{Fs}\right) - n_{TMD}\left(E_{Ci}, E_{Fi}\right)\right]\right) \quad (7)$$

Equation (7) needs to be constrained since it is possible to obtain any value of qV_{RTL} by varying E_C. Therefore, we constrain the amount of band bending in the TMDC layer due to charge transfer by requiring that the vacuum level be continuous from the source, across the RTLs and into the TMDC drain. This condition is enforced by (8) and (9), similar to the conditions used in [21].

$$q\,V_{RTL} = E_C - \chi_{TMD} \quad (8)$$

Since (8) and (7) are equal, we use them to obtain an equation for E_C which is given as (9).

$$E_C - \chi_{TMD} - \frac{q^2 t_{RTL}}{2\epsilon_0\epsilon_{RTL}}\left(2\left[n_{TMD}\left(E_C, E_{Fs}\right) - n_{TMD}\left(E_{Ci}, E_{Fi}\right)\right]\right) = 0 \quad (9)$$

Equation (9) is solved numerically and the resulting value of E_C is referred to as E_{C0}, which will be used as a reference value later when calculating the effects of gate and drain bias. E_{C0} is also fed back into (8) to determine $V_{RTL,0}$ which is the built-in voltage for electrons traversing the RTLs.

Next, we consider the effects of the applied drain and gate biases on the band structure of the device. We assume that the conduction band of the source is completely flat regardless of applied drain and gate bias due to degeneracy. When a drain bias, V_{drain}, is applied to the device, the voltage-drop over the RTLs will be equal to V_{drain}. This is because of the way in which we have setup our device, as can be seen in Fig. 2. Since the drain voltage is measured with respect to the source and the TMDC layer, the voltage-drop over the RTLs must be equal to V_{drain}. This in turn means that the conduction band position of the TMDC layer adjacent to the RTLs must be moved by qV_{drain} from its starting position of E_{C0}. Therefore, the voltage over the

RTLs when a drain bias is applied is given by (10).

$$q\,V_{RTL} = qV_{RTL,0} + qV_{drain} \tag{10}$$

There is also a voltage drop over the TMDC layer itself. Following the same method as described in [20], we will treat the TMDC layer as a thick plate with a uniform charge density and assume complete screening of the back-gate charge by the TMDC layer. In later calculations we will approximate the band bending of the TMDC layer as linear as was done in [20]. Using these assumptions, it is possible to derive (11) and (12) which describe the voltage drop over the TMDC layer (V_{TMD}) in terms of qV_{RTL} and qV_{gate}, where V_{gate} is the gate bias of the device and represents the total voltage drop over the TMDC and oxide layers. A full derivation of (11) and (12) is presented in Appendix A. Equation (11) describes the voltage drop over the TMDC layer if $qV_{RTL} > 0$ and (12) describes the voltage drop if $qV_{RTL} \leq 0$.

$$q\,V_{TMD} = qV_{RTL}\left(\frac{\epsilon_{RTL}t_{TMD}}{2\epsilon_{TMD}t_{RTL}}\right) - \left(qV_{gate}+qV_{RTL}\left(\frac{\epsilon_{RTL}t_{TMD}}{2\epsilon_{TMD}t_{RTL}}\right)\right)\left(1+\frac{2\epsilon_{TMD}t_{Oxide}}{\epsilon_{Oxide}t_{TMD}}\right)^{-1} \tag{11}$$

$$q\,V_{TMD} = qV_{RTL}\left(\frac{\epsilon_{RTL}t_{TMD}}{\epsilon_{TMD}t_{RTL}}\right) - \left(qV_{gate} + qV_{RTL}\left(\frac{\epsilon_{RTL}}{t_{RTL}}\right)\left(\frac{t_{TMD}}{\epsilon_{TMD}} + \frac{t_{Oxide}}{\epsilon_{Oxide}}\right)\right)\left(1 + \frac{2\epsilon_{TMD}t_{Oxide}}{\epsilon_{Oxide}t_{TMD}}\right)^{-1} \tag{12}$$

In (11) and (12) t_{RTL}, t_{TMD} and t_{Oxide} represent the total thickness of the resonant tunneling layers, the TMDC layer and the oxide layers respectively. ϵ_{Oxide} is the relative dielectric permittivity of the oxide layer while ϵ_{RTL} is the effective dielectric permittivity of the RTLs. It should also be noted that in our simulations qV_{gate} will be positive while qV_{RTL} will be negative. This is because qV_{gate} is measured with a positive test charge while qV_{RTL} is measured with a negative test charge. Further explanation of the sign conventions, as well as a derivation, for (11) and (12) is given in Appendix A.

The procedure for calculating the band structure of our device using (8)-(12) is straightforward. First, $qV_{RTL,0}$ is calculated using (8) and (9), then qV_{RTL} is calculated using (10) based on qV_{drain}. Next, the voltage-drop over the TMDC layer itself is calculated using (11) or (12) depending on the previously calculated value of qV_{RTL}. These steps can be repeated as needed for any combination of qV_{drain} and qV_{gate}.

Our method for calculating the tunneling probability for spin-polarized carriers is to use the well-established Transfer Matrix Method (TMM) with our calculated device band-structure. We based our TMM off of [32]–[34] and checked our code by reproducing the double barrier tunneling probability and current density vs. voltage (J-V) characteristics simulated in [32]. Equation (13) is used to calculate the J-V characteristics of our proposed device and is modified from [32], [35].

$$J = \frac{qm_{TMD}k_BT}{2\pi^2\hbar^3} \times \int_0^\infty T(E)\ln\left[\frac{1+Exp\left([E_{Fs}-E]/[k_BT]\right)}{1+Exp\left([E_{Fs}-E-q\left(V_{RTL}+V_{TMD}\right)]/[k_BT]\right)}\right]dE \tag{13}$$

In (13), we have replaced V_a in [32], [35] with $V_{RTL} + V_{TMD}$, because the total voltage drop experienced by a carrier moving from the semiconductor source all the way into the TMDC layer is $V_{RTL} + V_{TMD}$ instead of simply the applied drain bias (qV_{RTL}). $T(E)$ is the probability of tunneling, or transmission coefficient, with respect to the energy of the carrier measured relative to the conduction band of the source. Using (13) in conjunction with the TMM and (8)-(12) to calculate $T(E)$, the spin-polarized current through our proposed device can be calculated.

Few-layer CrI_3 was determined to have an effective carrier mass of 13.18 m_e, and an electron affinity of approximately 4.3 eV based off of data from [36]. From [36], we also determined the exchange energy, E_{ex}, to be 0.07 eV. This is a far lower value of E_{ex} than what was reported in [13], [37], [38]. Details of our I-V analysis of the data from [36] and how we arrived at our reported values of m_e, χ and E_{ex} for CrI_3 can be found in Appendix B. The relative permittivity of CrI_3 is taken as 1.8 and comes from [12], [39].

In our device design, the semiconductor source is $In_xGa_{1-x}N$, the properties of which are reported with χ ranging from 4-5.6 eV and the effective mass ranging from 0.2-0.05 m_e [40]. The equations describing how the electron affinity and effective mass change with Indium composition are given in [40]. For h-BN, an electron affinity of approximately 2 eV and an effective mass of 0.26 m_e are used in our calculations and come from [41]–[44]. The relative dielectric permittivity of h-BN is taken as 3.29 [45]. The effective dielectric constant for the RTLs (ϵ_{RTL}) can be calculated using (21) in Appendix A. For the double h-BN barrier device shown in Fig. 1, $\epsilon_{RTL} = 2.28$. If we remove the second h-BN layer in Fig. 1 then we have the single barrier device which has a slightly different effective dielectric constant of $\epsilon_{RTL}= 2.08$. The insulating layer for the back-gate in our device is Al_2O_3 which has a relative dielectric permittivity of 9 [46]. The position of the Al_2O_3 conduction band in Fig. 1 was based on its electron affinity which was determined in [47].

The electron affinity of MoS_2 is assumed to be 4.5 eV, which is a compromise value based on [48] and [49]. However, as carriers move from the CBM of the $In_xGa_{1-x}N$ layer, which is at the Γ-point of the $In_xGa_{1-x}N$ Brillouin Zone (BZ), they do not have time to scatter and so end up at the Γ-point of the MoS_2 band structure. It is possible that the carriers could scatter through the RTLs in order to reach the K-point (and thus CBM) of the MoS_2 layer, but in our calculations this possibility is ignored. Therefore, our tunneling and current density calculations are likely to underestimate both the probability of carrier tunneling as well as the total current density since we ignore scattering. In order to reflect that the carriers are tunneling into the Γ-point

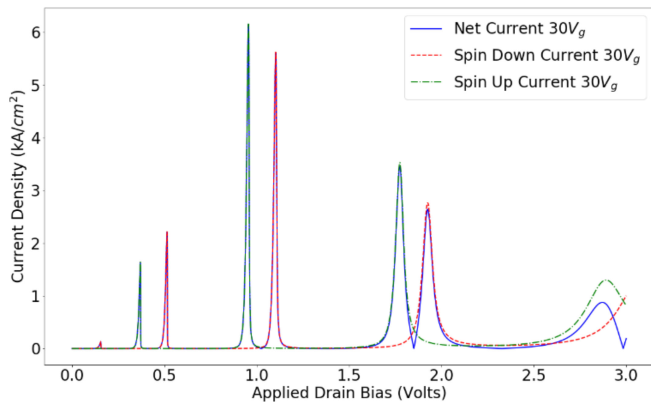

Fig. 3. Current density (kA/cm^2) vs. Applied Drain Bias (Volts) for the double h-BN barrier spin-RTD with $30\boldsymbol{V_{gate}}$. CrI_3 is polarized in the $+$y direction meaning $|\uparrow\rangle$ carriers would be preferred without resonant tunneling.

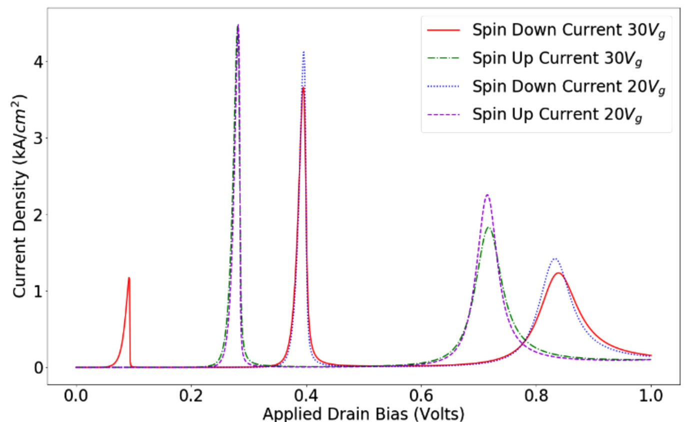

Fig. 4. Current density (kA/cm^2) vs. Applied Drain Bias (Volts) for the single h-BN barrier spin-RTD with $30\boldsymbol{V_{gate}}$ and $20\boldsymbol{V_{gate}}$. CrI_3 is polarized in the $+$y direction meaning $|\uparrow\rangle$ carriers would be preferred without resonant tunneling.

of the MoS_2, we must know the energy difference between the K-point and Γ-point in MoS_2 as well as the effective mass at the Γ-point. Using the results from Materials Cloud [50], we get a difference in energy between the K-point and Γ-point of 1.12 eV and therefore an estimated Γ-point electron affinity of 3.38 eV for MoS_2. The effective mass of MoS_2 at the Γ-point is taken to be 0.76 m_e based on DFT calculations in [51].

It should also be noted that detailed calculations carried out by [52] have shown that tunneling through the Γ-point is preferred at low applied bias in MoS_2. Although the authors of [52] were studying the operation of an MTJ made of alternating layers of VSe_2 and MoS_2, their detailed calculations lend credibility to our assumption that the carriers in a vdW heterostructure will preferentially tunnel through the Γ-point.

The thickness of the TMDC and CrI_3 layers are both assumed to be 0.7 nm in thickness [38], [48], while the h-BN and Al_2O_3 layers are assumed to be 0.3 nm and 10 nm thick respectively [46], [53]. For the fabrication of the device described in Fig. 2, interested readers can refer to papers such as [54].

The electrostatic gating of CrI_3 can potentially change the value of E_{ex} according to experimental results [55], [56]. We estimate that the E_{ex} can decrease by approximately 20% with an increase in the applied gate voltage of 30 Volts, based on [55], [57]. Although significant, this decrease does not invalidate the proposed device, and it simply requires that the device be operated at a higher drain bias and a lower gate voltage. It should also be noted that the E_{ex} value we use is lower than that of other authors [13].

IV. Simulation Results

Our first set of results are for the double h-BN barrier device. In this device, shown in Fig. 1 and Fig. 3, the h-BN layers serve to create sharp well defined resonant tunneling states by making the resonant tunneling well extremely narrow with high barriers. By making the resonant tunneling states narrower in terms of energy, it is possible to have much more highly spin polarized currents. We have also selected the electron affinity of the source as 4.1 eV by choosing the source to be $In_{0.11}Ga_{0.89}N$. From Fig. 3, it is obvious that the resulting spin-polarized currents are highly spin-polarized with almost no overlap between different resonant spin currents.

If we remove the second h-BN layer seen in Fig. 1. from our device, then we obtain the results shown in Fig. 4. In Fig. 4, the single barrier device has far higher current density at lower applied drain bias when compared to the double-barrier device. Also, in Fig. 4 the first current peak is $|\downarrow\rangle$, which means that our proposed device can preferentially inject minority carriers into the TMDC layer with an appropriate gate voltage. If the gate voltage is lower, then $|\downarrow\rangle$ carriers are unable to tunnel from the nitride layer into the TMDC due to insufficient conduction band bending in the TMDC layer. The change in the J-V characteristics is seen in Fig. 4 for currents at $20V_{gate}$.

From Fig. 4, it can be seen that the proposed device can theoretically switch between injecting $|\downarrow\rangle$ and $|\uparrow\rangle$ polarized carriers into MoS_2 by varying the gate voltage. Although this method of spin-injection is likely to be less efficient than a standard MTJ for injecting the majority spin state, it does demonstrate another possible advantage of this device concept. This switching occurs in our simulated J-V data as the gate voltage bends the conduction band of the MoS_2 downwards over the width of the MoS_2 layer. In a real device, the effect of the back-gate would likely not be as dramatic, but it would still affect the measured current density as shown by [20] and [21]. Another important observation about our simulated tunnel currents is that they are extremely narrow and that the results are most accurate at low applied drain bias.

V. Conclusion

From our calculations, it is clear that a spin-RTD with the ability to select the polarization of carriers through all electric means is theoretically possible. Furthermore, based on Figs. 3 & 4, it should be possible to use resonant tunneling to select minority spin-polarized carriers over majority spin-polarized carriers in either of the devices proposed. Advantages of our proposed device over previous spin-RTDs [9]–[11], which used

thin films of magnetic semiconductors and had operation temperatures within the range of 1.3K to 8K, include larger spin splitting, higher operating temperature, and better control over the spin polarization of carriers. Our proposed device is also unique in that it allows for an all-electrical control of spin injection into monolayer MoS_2 and could potentially be extended to other TMDCs. The proposed spin-RTD can be used in quantum computing and other low-temperature applications such as spintronics and valleytronics, and as such the low Curie temperature of single-layer CrI_3 is not an issue.

Appendix A

To derive (11) and (12) we must determine the total potential across the oxide and TMDC layers, V_{gate}, in our device in terms of V_{RTL} and V_{gate} which are known. To do so, we need to know the how charge is distributed initially between the source and the TMDC layer and the response of the system when new charges are added/removed to the gate. These two sets of charges can have their contribution to V_{gate} broken into separate potentials as done in (14).

$$q\,V_{gate} = q\left(V_{TMD,0} + V_{Oxide,0} + V_{TMD,g} + V_{Oxide,g}\right) \tag{14}$$

$V_{TMD,0}$ and $V_{Oxide,0}$ are the potentials across the TMDC and oxide layers when no charge is present on the back-gate, while $V_{TMD,g}$ and $V_{Oxide,g}$ are the potentials across those layers due to charges added to back-gate. The form of $V_{TMD,0}$ and $V_{Oxide,0}$ depend on the sign of qV_{RTL}. We will first consider the case of when $qV_{RTL} > 0$ from an electron's perspective. We will assume that there is a uniform negative charge, n_{TMD}, on the TMDC layer and an equal and opposite charge on the source, n_{Source}. This is in line with the assumptions made in Section III. Treating the TMDC layer and the source as thick charged parallel plates and the RTL as an insulating layer we can calculate qV_{RTL} and $qV_{TMD,0}$. $qV_{Oxide,0}$ is zero because $n_{TMD} + n_{Source} = 0$.

$$q\,V_{RTL} = \frac{q^2 t_{RTL}}{\epsilon_0 \epsilon_{RTL}}\, n_{TMD},\; q\,V_{TMD,0} = \frac{q^2 t_{TMD}}{2\epsilon_0 \epsilon_{TMD}}\, n_{TMD} \tag{15}$$

Solving for n_{TMD} in terms of qV_{RTL} we can substitute that expression into $qV_{TMD,0}$ and solve for $qV_{TMD,0}$ in terms of qV_{RTL} which gives us (16).

$$qV_{TMD,0} = qV_{RTL}\left(\frac{\epsilon_{RTL} t_{TMD}}{2\epsilon_{TMD} t_{RTL}}\right) \tag{16}$$

Next, we consider what happens if $qV_{RTL} \le 0$. Since we cannot have a positive charge build up on the TMDC layer without unreasonable band bending we will instead assume that all the charge needed to produce qV_{RTL} come from negative charges on the source. Using the same assumptions as were used for (15) but with $n_{TMD} \approx 0$ we can derive a similar set of equations for $qV_{TMD,0}$ and $qV_{Oxide,0}$, which is no longer zero, in terms of the dielectric constants and n_{Source}. Solving for n_{Source} in terms of qV_{RTL} and performing some algebra we arrive at (30).

$$\begin{aligned} qV_{TMD,0} &= qV_{Oxide,0}\left(\frac{t_{TMD}\epsilon_{Oxide}}{t_{Oxide}\epsilon_{TMD}}\right) \\ &= qV_{RTL}\left(\frac{\epsilon_{RTL}}{t_{RTL}}\right)\left(\frac{t_{TMD}}{\epsilon_{TMD}}\right) \end{aligned} \tag{17}$$

Now that we have expression for $qV_{TMD,0}$ and $qV_{Oxide,0}$ for when $qV_{RTL} > 0$ and $qV_{RTL} \le 0$ we can now move onto deriving expressions for $qV_{TMD,g}$ and $qV_{Oxide,g}$. We will assume that the TMDC layer completely screens any charges added to the back-gate, $n_{TMD} = -n_{gate}$, which is the same as was done in [20]. Therefore, treating the TMDC and back-gate as thick uniformly charged plates in a capacitor we get (18).

$$\begin{aligned} q\,V_{TMD,g} &= qV_{Oxide,g}\left(\frac{\epsilon_{Oxide} t_{TMD}}{2\epsilon_{TMD} t_{Oxide}}\right) \\ &= \frac{q^2 t_{TMD}}{2\epsilon_0 \epsilon_{TMD}}\,(n_{TMD}) \end{aligned} \tag{18}$$

Using (18) it is possible to re-write $qV_{Oxide,g}$ in terms of $qV_{TMD,g}$. Since qV_{TMD} is the sum of $qV_{TMD,0}$ and $qV_{TMD,g}$ we now have everything we need in order to solve for qV_{TMD} in terms of qV_{RTL} and qV_{gate}. It is worth noting that since $q\,V_{TMD} = qV_{TMD,0} + qV_{TMD,g}$ that $q\,V_{TMD,g} = qV_{TMD} - qV_{TMD,0}$, this is an important consideration during the algebra. Using (14), (16) and (18) for $qV_{RTL} > 0$ and (14), (17) and (18) for $qV_{RTL} \le 0$, we can solve for qV_{TMD} in terms of qV_{RTL} and qV_{gate}. After some algebraic manipulation, this gives us (11) and (12). Regarding sing conventions, it should be noted that qV_{gate} is measured with a positive test charge while qV_{RTL} is measured with a negative one. Therefore, qV_{gate} needs to be multiplied by -1 to obtain (11) and (12).

To derive an expression for ϵ_{RTL}, we first treat the source and TMDC layers as parallel plates with arbitrary charge densities σ_{Source} and σ_{TMD} respectively. Next, we write down an expression for the total potential drop over the RTL (19)

$$\begin{aligned} V_{RTL} = {} & n t_{hBN}\left(\frac{\sigma_{Source} + \sigma_{TMD}}{2\epsilon_{hBN}}\right) \\ & + t_{CrI_3}\left(\frac{\sigma_{Source} + \sigma_{TMD}}{2\epsilon_{CrI_3}}\right) \end{aligned} \tag{19}$$

Where *n* is the number of h-BN layers in the device. We then substitute in an effective dielectric with a relative permittivity of ϵ_{RTL} in place of the h-BN and CrI_3 layers. This gives us (20).

$$V_{RTL} = (n t_{hBN} + t_{CrI_3})\left(\frac{\sigma_{Source} + \sigma_{TMD}}{2\epsilon_{RTL}}\right) \tag{20}$$

Setting these two equations equal and solving for ϵ_{RTL} we get (21).

$$\epsilon_{RTL} = \frac{(n t_{hBN} + t_{CrI_3})\,\epsilon_{CrI_3}\epsilon_{hBN}}{(n t_{hBN}\epsilon_{CrI_3} + t_{CrI_3}\epsilon_{hBN})} \tag{21}$$

The results of (21) for the double barrier device ($n = 2$) is $\epsilon_{RTL} = 2.28$ and for the single barrier device ($n = 1$) is $\epsilon_{RTL} = 2.08$.

Appendix B

We preformed our own analysis of the IV data from [36] to determine relevant properties of CrI_3 such as E_{ex}, m_e, and χ. DFT calculations performed in [58], [59] showed m_e ranges from 5 m_e to 27 m_e for CrI_3. Although we don't expect DFT calculations to perfectly predict the true effective mass of CrI_3, we do expect them to be accurate to within an order of magnitude. Therefore, we decided to perform our own analysis to determine E_{ex}, m_e, and χ. Our analysis of the IV data from [36] centered around the Fowler-Nordheim (FN) tunneling regime, similar to the analysis done in [13], [37], [38] but we used Simmon's theory of tunneling [60] instead of the FN equations.

In the CrI_3 device, the tunneling layers are treated as having alternating barrier heights based on their magnetic alignment, and such device concepts have been discussed previously [57]. To analyze the I-V data using [60], we plotted $1/V vs.\ \ln(J/V^2)$. which is a linear relationship (at high drain bias) and thus easy to fit.

We chose what voltage range to fit based on visual inspection. Carrying out this procedure for the 2-layer and 4-layer devices in [36], we were able to obtain a set of fit values. From these fit values, it was possible to determine the carrier effective mass and spin-dependent barrier heights from the data. 3-layer devices were not been included in the analysis, because it was not possible to determine their barrier alignments for the AFM case from the I-V data. However, for 2-layer and 4-layer CrI_3 devices the FM/AFM ordering was obvious due to symmetry. When fitting the data, constraints were placed on the effective mass and the FM/AFM barrier heights such as $\varphi_{AFM} > \varphi_{FM}$, $\varphi_{AFM} > 0$, $\varphi_{AFM}\langle 0.25,\ \varphi_{FM}\rangle 0$, $m_e\langle 50,\ m_e\rangle 0$.

These restrictions prevented the fitting process from producing unrealistic values of the effective mass and barrier heights. We obtained an effective mass of $13.1812 m_e$, an AFM barrier height of $0.1812\ eV$ and a FM barrier height of $0.1504\ eV$. Recalling that φ_{AFM} is the average of the minority and majority barrier heights [60] then it is possible to extract the minority barrier height by solving $\varphi_{AFM} = 0.5(\varphi_{|\uparrow\rangle} + \varphi_{|\downarrow\rangle})$. Doing so, we obtain a value of $0.2192\ eV$ for $\varphi_{|\downarrow\rangle}$. This lets us calculate the E_{ex} as $\varphi_{|\uparrow\rangle} - \varphi_{|\downarrow\rangle}$ that gives $0.06883\ eV$ which we approximated as 0.07 eV.

Based on the bandgap of CrI_3 and its estimated electron affinity, we assumed this effective mass must be that of the electron. The estimated electron affinity of CrI_3 ranges from 4.3 eV [61] to 4.48 eV in [62]. In [38], a bandgap of 1.2 eV was determined by photoluminescence. Since graphene has a work function between 4.5 eV and 4.56 eV [44], [63] and our $\varphi_{AFM} = 0.1812\ eV$, then an electron affinity of 4.3 eV seems reasonable and would seem to imply electron tunneling in the devices.

Acknowledgment

The authors would like to thank Prof. Michael Stroscio for the many inspiring discussions. They would also like to thank Kim from the University of Waterloo for his helpful email discussions regarding tunneling in CrI_3.

References

[1] B. Behin-Aein *et al.*, "Proposal for an all-spin logic device with built-in memory," *Nature Nanotechnol.*, vol. 5, no. 4, pp. 266–270, 2010.

[2] X. Liu and M. C. Hersam, "2D materials for quantum information science," *Nature Rev. Mater.*, vol. 4, no. 10, pp. 669–684, 2019.

[3] M. Galbiati *et al.*, "Path to overcome material and fundamental obstacles in spin valves based on MoS_2 and other transition-metal dichalcogenides," *Phys. Rev. Appl.*, vol. 12, no. 4, 2019.

[4] S. Liang *et al.*, "Electrical spin injection and detection in molybdenum disulfide multilayer channel," *Nature Commun.*, vol. 8, no. 1, 2017, Art. no. 14947.

[5] A. Fert and H. Jaffrès, "Conditions for efficient spin injection from a ferromagnetic metal into a semiconductor," *Phys. Rev. B*, vol. 64, no. 18, 2001.

[6] G. Schmidt *et al.*, "Fundamental obstacle for electrical spin injection from a ferromagnetic metal into a diffusive semiconductor," *Phys. Rev. B*, vol. 62, no. 8, pp. R4790–R4793, 2000.

[7] G. Sallen *et al.*, "Robust optical emission polarization in MoS_2 monolayers through selective valley excitation," *Phys. Rev. B*, vol. 86, no. 8, 2012, Art. no. 081301.

[8] D. Zhong *et al.*, "Van der Waals engineering of ferromagnetic semiconductor heterostructures for spin and valleytronics," *Sci. Adv.*, vol. 3, no. 5, 2017, Art. no. e1603113.

[9] A. Slobodskyy *et al.*, "Voltage-controlled spin selection in a magnetic resonant tunneling diode," *Phys. Rev. Lett.*, vol. 90, no. 24, 2003, Art. no. 246601.

[10] D. Sanchez *et al.*, "Spin-polarized transport in II-VI magnetic resonant-tunneling devices," *Ted*, vol. 54, no. 5, pp. 984–990, 2007.

[11] Z. L. Fang *et al.*, "Spin-dependent resonant tunneling through 6μm diameter double barrier resonant tunneling diode," *Appl. Phys. Lett.*, vol. 91, no. 2, Art. no. 022101, 2007.

[12] B. Huang *et al.*, "Layer-dependent ferromagnetism in a van der Waals crystal down to the monolayer limit," *Nature*, vol. 546, no. 7657, pp. 270–273, 2017.

[13] H. H. Kim *et al.*, "Tailored tunnel magnetoresistance response in three ultrathin chromium trihalides," *Nano Lett.*, vol. 19, no. 8, pp. 5739–5745, 2019.

[14] L. Ciorciaro *et al.*, "Observation of magnetic proximity effect using resonant optical spectroscopy of an electrically tunable $MoSe_2/CrBr_3$ heterostructure," *Phys. Rev. Lett.*, vol. 124, no. 19, 2020, Art. no. 197401.

[15] Z. Zhang *et al.*, "Direct photoluminescence probing of ferromagnetism in monolayer two-dimensional CrBr3," *Nano Lett.*, vol. 19, no. 5, pp. 3138–3142, 2019.

[16] T. Kümmell *et al.*, "Carrier transfer across a 2D-3D semiconductor heterointerface: The role of momentum mismatch," *Phys. Rev. B*, vol. 95, no. 8, 2017.

[17] B. Li *et al.*, "3D band diagram and photoexcitation of 2D–3D semiconductor heterojunctions," *Nano Lett.*, vol. 15, no. 9, pp. 5919–5925, 2015.

[18] H. Henck *et al.*, "Interface dipole and band bending in the hybrid P-N heterojunction MoS_2/GaN(0001)," *Phys. Rev. B*, vol. 96, no. 11, 2017, Art. no. 115312.

[19] H. Jeong *et al.*, "Semiconductor–insulator–semiconductor diode consisting of monolayer MoS_2, h-BN, and GaN heterostructure," *ACS Nano*, vol. 9, no. 10, 2015, Art. no. 10032-10038.

[20] A. Prakash *et al.*, "Understanding contact gating in Schottky barrier transistors from 2D channels," *Scientific Reports*, vol. 7, no. 1, 2017, Art. no. 12596.

[21] T. S. Ghiasi, J. Quereda, and B. J. van Wees, "Bilayer h-BN barriers for tunneling contacts in fully-encapsulated monolayer $MoSe_2$ field-effect transistors," *2D Mater.*, vol. 6, no. 1, 2019, Art. no. 015002.

[22] A. Szabó *et al.*, "Electron Transport through Metal/MoS_2 Interfaces: Edge- or Area- Dependent process?," *Nano. Lett.*, vol. 19, pp. 3641–3647, 2019.

[23] W. Zhu *et al.*, "Nanoscale electronic devices based on transistion metal dichalcogenides," *2D Mater.*, vol. 6, no. 3, 2019, Art. no. 032004.

[24] S. Krishnamoorthy *et al.*, "High current density 2D/3D MoS_2/GaN Esaki tunnel diodes," *Appl. Phys. Lett.*, vol. 109, no. 18, 2016, Art. no. 183505.

[25] K. Xu, Y. Cai, and W. Zhu, "Esaki diodes based on 2-D/3-D heterojunctions," *IEEE Trans. Electron. Devices*, vol. 65, no. 10, pp. 4155–4159, Oct. 2018.

[26] S. Shokhovets *et al.*, "Observation of Fermi-edge excitons and exciton-phonon complexes in the optical response of heavily doped n-type wurtzite GaN," *Phys. Rev. B*, vol. 79, no. 4, 2009, Art. no. 045201.

[27] M. Feneberg *et al.*, “Band gap renormalization and Burstein-Moss effect in silicon- and germanium-doped wurtzite GaN up to 1020 cm-3,” *Phys. Rev. B*, vol. 90, no. 7, 2014, Art. no. 075203.
[28] A. Ajay et al*et al.*, “Ge doping of GaN beyond the Mott transition,” *J. Phys. D*, vol. 49, no. 44, 2016, Art. no. 445301.
[29] K. Ueno *et al.*, “Electron transport properties of degenerate N-type GaN prepared by pulsed sputtering,” *APL Mater.*, vol. 5, no. 12, 2017, Art. no. 126102.
[30] P. Pampili and P. J. Parbrook, “Doping of III-nitride materials,” *Mater. Sci. Semicond. Process.*, vol. 62, pp. 180–191, 2017.
[31] N. Ma and D. Jena, “Carrier statistics and quantum capacitance effects on mobility extraction in two-dimensional crystal semiconductor field-effect transistors,” *2D Mater.*, vol. 2, no. 1, 2015, Art. no. 015003.
[32] S. Vatannia and G. Gildenblat, “Airy’s functions implementation of the transfer-matrix method for resonant tunneling in variably spaced finite superlattices,” *IEEE J. Quant. Electron.*, vol. 32, no. 6, pp. 1093–1105, Jun. 1996.
[33] C. Jirauschek, “Accuracy of transfer matrix approaches for solving the effective mass Schrödinger equation,” *IEEE J. Quant. Electron.*, vol. 45, no. 9, pp. 1059–1067, Sep. 2009.
[34] W. Li, “Generalized free wave transfer matrix method for solving the schrödinger equation with an arbitrary potential profile,” *IEEE J. Quantum Electron.*, vol. 46, no. 6, pp. 970–975, 2010.
[35] R. Tsu and L. Esaki, “Tunneling in a finite superlattice,” *Appl. Phys. Lett.*, vol. 22, no. 11, pp. 562–564, 1973.
[36] T. Song *et al.*, “Giant tunneling magnetoresistance in spin-filter van der Waals heterostructures,” *Science*, vol. 360, no. 6394, pp. 1214–1218, 2018.
[37] H. H. Kim *et al.*, “One million percent tunnel magnetoresistance in a magnetic van der waals heterostructure,” *Nano Lett.*, vol. 18, no. 8, pp. 4885–4890, 2018.
[38] Z. Wang *et al.*, “Very large tunneling magnetoresistance in layered magnetic semiconductor CrI3,” *Nature Commun.*, vol. 9, no. 1, 2018, Art. no. 2516.
[39] K. Zollner, P. E. Faria Junior, and J. Fabian, “Proximity exchange effects in $MoSe_2$ and WSe_2 heterostructures with CrI_3: Twist angle, layer, and gate dependence,” *Phys. Rev. B*, vol. 100, no. 8, 2019, Art. no. 085128.
[40] G. F. Brown *et al.*, “Finite element simulations of compositionally graded InGaN solar cells,” *Solar Energy Mater. Solar Cells*, vol. 94, pp. 478–483, 2010.
[41] G. Lee *et al.*, “Electron tunneling through atomically flat and ultrathin hexagonal boron nitride,” *Appl. Phys. Lett.*, vol. 99, no. 24, 2011, Art. no.. 243114-3.
[42] W. M. H. Sachtler, G. J. H. Dorgelo and A. A. Holscher, “The work function of gold,” *Surface Sci.*, vol. 5, no. 2, pp. 221–229, 1966.
[43] G. Cassabois, P. Valvin and B. Gil, “Hexagonal boron nitride is an indirect bandgap semiconductor,” *Nature Photon.*, vol. 10, no. 4, pp. 262–266, 2016.
[44] V. K. Sangwan and M. C. Hersam, “Electronic transport in two-dimensional materials,” *Annu. Rev. Phys. Chem.*, vol. 69, no. 1, pp. 299–325, 2018.
[45] A. Laturia, M. L. Van de Put, and W. G. Vandenberghe, “Dielectric properties of hexagonal boron nitride and transition metal dichalcogenides: from monolayer to bulk,” *2D Mater. Appl.*, vol. 2, no. 1, 2018, Art. no. 6.
[46] J. Robertson, “High dielectric constant oxides,” *Eur. Phys. J. Appl. Phys.*, vol. 28, pp. 265–291, 2004.
[47] M. L. Huang *et al.*, “Energy-band parameters of atomic-layer-deposition Al_2O_3/InGaAs heterostructure,” *Appl. Phys. Lett.*, vol. 89, no. 1, 2006, Art. no. 012903.
[48] S. L. Howell *et al.*, “Investigation of band-offsets at monolayer–multilayer MoS_2 junctions by scanning photocurrent microscopy,” *Nano Lett.*, vol. 15, no. 4, pp. 2278–2284, 2015.
[49] D. H. Kim and D. Lim, “The electrical and valley properties of monolayer $MoSe_2$,” *Current Appl. Phys.*, vol. 17, no. 2, pp. 321–325, 2017.
[50] N. Mounet *et al.*, “Two-dimensional materials from high-throughput computational exfoliation of experimentally known compounds,” *Nature Nanotechnol.*, vol. 13, no. 3, pp. 246–252, 2018.
[51] E. Ridolfi *et al.*, “A tight-binding model for MoS_2 monolayers,” *J. Phys.: Condensed Matter*, vol. 27, no. 36, 2015, Art. no. 365501.
[52] J. Zhou *et al.*, “Large tunneling magnetoresistance in VSe_2/MoS_2 magnetic tunnel junction,” *ACS Appl. Mater. Interfaces*, vol. 11, no. 19, pp. 17647–17653, 2019.
[53] D. Golla *et al.*, “Optical thickness determination of hexagonal boron nitride flakes,” *Appl. Phys. Lett.*, vol. 102, no. 16, 2013, Art. no. 161906.
[54] P. J. Zomer *et al.*, “Fast pick up technique for high quality heterostructures of bilayer graphene and hexagonal boron nitride,” *Appl. Phys. Lett.*, vol. 105, no. 1, 2014, Art. no. 013101.
[55] S. Jiang *et al.*, “Controlling magnetism in 2D CrI_3 by electrostatic doping,” *Nature Nanotechnol.*, vol. 13, no. 7, pp. 549–553, 2018.
[56] T. Song *et al.*, “Voltage control of a van der Waals spin-filter magnetic tunnel junction,” *Nano Lett.*, vol. 19, no. 2, pp. 915–920, 2019.
[57] D. C. Worledge and T. H. Geballe, “Magnetoresistive double spin filter tunnel junction,” *J. Appl. Phys.*, vol. 88, no. 9, pp. 5277–5279, 2000.
[58] S. Haastrup *et al.*, “The computational 2D materials database: High-throughput modeling and discovery of atomically thin crystals,” *2D Mater.*, vol. 5, no. 4, 2018, Art. no. 042002.
[59] C. Lin *et al.*, “Enhanced valley splitting of transition-metal dichalcogenide by vacancies in robust ferromagnetic insulating chromium trihalides,” *ACS Appl. Mater. Interfaces*, vol. 11, no. 20, pp. 18858–18864, 2019.
[60] J. G. Simmons, “Generalized formula for the electric tunnel effect between similar electrodes separated by a thin insulating film,” *J. Appl. Phys.*, vol. 34, no. 6, pp. 1793–1803, 1963.
[61] T. R. Paudel and E. Y. Tsymbal, “Spin filtering in CrI_3 tunnel junctions,” *ACS Appl. Mater. Interfaces*, vol. 11, no. 17, pp. 15781–15787, 2019.
[62] J. Zhang *et al.*, “Strong magnetization and Chern insulators in compressed graphene/CrI_3 van der Waals heterostructures,” *Phys. Rev. B*, vol. 97, no. 8, 2018, Art. no. 085401.
[63] R. Yan *et al.*, “Determination of graphene work function and graphene-insulator-semiconductor band alignment by internal photoemission spectroscopy,” *Appl. Phys. Lett.*, vol. 101, no. 2, 2012, Art. no. 022105.

John Eric Tiessen was born in St. Paul Minnesota, United States, in 1993. He received **the** B.S. degree in physics from Valparaiso University, Valparaiso Indiana, United States, in 2016 and the M.S. degree in Physics from the University of Illinois at Chicago, Chicago, Illinois, in 2019.

He is currently working with the Advanced Semiconductor and Materials Laboratory, University of Illinois at Chicago. He is working toward the Ph.D. degree under the direction of Dr. Junxia Shi.

Junxia Shi (Senior Member, IEEE) received the Ph.D. degree in electrical engineering from Cornell University, Ithaca, NY, in 2010. She is currently an Associate Professor with the Department of Electrical and Computer Engineering, University of Illinois at Chicago. She has authored and coauthored more than 70 articles and patents. Her research focuses on advanced compound semiconductor materials and devices, including gallium nitride-based power and RF devices, group III-V terahertz photodetectors, and TMDC 2D nanostructure-based valleytronics, qubits, chemical and biological sensors, etc. Professor Shi is a Senior Member of the IEEE.